On the synthesis and design of a novel backdrivable high-stiffness capstan drive

Jordan M. Longval and Clément Gosselin

Abstract—This article introduces a novel backdrivable high-stiffness cable capstan drive architecture for robotics applications. The drive has a low transmission ratio and a higher stiffness than typical capstan drives. The higher transmission stiffness is obtained by the use of grooves on both the input and the output pulleys of the drive which increases the effective coefficient of friction between the pulleys and the cable. The groove on the input pulley forms a single helix while the grooves on the output pulley form a R-helix, where R is equal to the transmission ratio of the drive. This property enables several different multi-cable arrangements for the drive, which further increases the transmission stiffness. A kinematic model of the capstan drive is established and used to ensure the proper alignment of the input pulley groove and output pulley grooves as a function of the distance between the pulleys. A 3D printed prototype of the transmission is presented.

Index Terms—backdrivable, transmission, robot, cable, capstan, collaboration

I. INTRODUCTION

ROBOTIC manipulators typically use transmissions with large reduction ratios in order to reduce the size and mass of the actuators. Such transmissions (e.g. harmonic drives) are not backdrivable, which is a limitation in some applications. For example, in Collaborative Robots (CR), it is desired to provide physical Human-Robot Interaction (pHRI), i.e., to allow users to manipulate the robot links directly.

Because their transmissions are not backdrivable, most CR used nowadays require force sensors to enable task teaching through pHRI. The force sensors are either placed near the CR's end effector [1] [2] [3] or inside each joint of the CR through the use of strain gauges [4]. The use of force/torque sensors limits the bandwidth of the pHRI and makes the interaction less intuitive and agile.

It is possible to teach CR tasks through pHRI without using force sensors. To this end, alternative robot kinematic architectures coupled with backdrivable Low-Ratio Transmissions (LRT) can be used. Alternative robot kinematic architectures can be used to move the CR actuators toward the base in order to minimize the influence of their inertia on the robot dynamics and payload capabilities while allowing larger and stronger actuators with backdrivable transmissions. This concept is already used in industrial palletizing robots [5], haptic devices [6] and backdrivable pHRI robots [7] [8].

LRT are already used in haptic devices for telesurgery [9] [10] [11] [12]. Yet, not all LRT are mechanically backdrivable. For example, a worm gear cannot be driven by its output

J. Longval and C. Gosselin are with the Department of Mechanical Engineering, Université Laval, Québec, Canada e-mail:gosselin@gmc.ulaval.ca.

table

TABLE I
COMPARISON OF DIFFERENT BACKDRIVABLE LRT.

LRT type	Advantages	Disadvantages
Spur and helical gears	High stiffness High torque capability	Clearance between teeth (backlash)
Belt drive	Transmission over a larger distance No backlash	Lower stiffness Slip error
Chain Drive	High stiffness	Clearance between inner links Higher transmission inertia
Cable (capstan drive)	Higher stiffness than belt drive No backlash	Lower stiffness than chain and gears Slip error

(through the worm).Table I shows a list of backdrivable LRT and indicates their advantages and disadvantages for pHRI.

Table I shows that a capstan drive is a good choice of backdrivable LRT because it has higher stiffness than a belt drive and it has a low backlash like gears or chain drives. This is why it is used in haptic devices [10] [13], highly backdrivable collaborative robots [14] [15] [16] and high precision targeting systems [17] [18] [19] [20]. Having low backlash is very important for robotics applications which require the robot's motors to work in both directions at a high frequency [21] [22]. However, Table I also shows that capstan drives have lower stiffness than other LRT such as gears and can be subject to slip error [19] [23].

In order to alleviate these drawbacks, this article presents a novel capstan architecture that increases the stiffness of the transmission by using grooves on the transmission's pulleys. The grooves increase the friction coefficient between the cable and the pulleys, which makes the transmission stiffer. Moreover, the novel capstan drive allows multiple cable arrangements, which further increases the stiffness of the transmission.

This paper is structured as follows. In Section II and III, the general modelling of a capstan drive and its torsional stiffness are recalled. The theoretical model used here is based on the work of Werkmeister et al. [24]. Part of this model is also used in [23]. Section IV explains how grooves etched along the surface of a capstan drive's pulleys can theoretically increase the friction coefficient between the drive's cable and its pulleys thus increasing the overall stiffness of the capstan drive. The use of grooves in capstan drives has already been presented in [18]. However, this paper presents a novel design for the output pulley of a capstan drive which uses grooves arranged
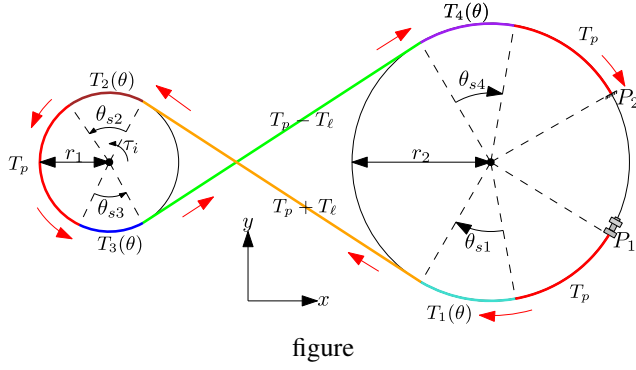
figure

Fig. 1. Modelling of a capstan drive.

figure

Fig. 2. Small segment of the cable pulley interaction.

as a multiple helix. This novel design enables different multi-cable arrangements of the capstan drive that can theoretically further increase its torsional stiffness. The novel capstan drive architecture as well as different possible cable arrangements are presented in Section V. The advantages and disadvantages of each of the proposed arrangements are discussed. Section VI then proposes a method to properly arrange the capstan drive's pulleys during the drive's assembly so that the cables can follow a smooth and continuous path while passing from one pulley to the other. Finally, concluding remarks are made in Section VIII.

II. MODELLING OF A CAPSTAN DRIVE

Figure 1 presents the different elements of the capstan drive model. In figure 1, r_1 is the radius of the small input pulley while r_2 is the radius of the large output pulley. The transmission ratio is given by $R = \frac{r_2}{r_1}$. The cable passes from the large pulley to the small pulley and back to the large pulley in a lemniscate shaped pattern indicated by the red arrows in figure 1. A preload tension T_p is applied on the cable by pulling on the cable with a mechanism alike a turnbuckle (at point P_1) and by fixing the other end of the cable to the pulley(at point P_2).

When a torque τ_i is applied on the input pulley, one side of the cable extends while the other part of the cable shortens. The extension is caused by an increase in the tension in the cable by an amount T_ℓ while the contraction of the other part of the cable is caused by a reduction of the tension by an equal amount T_ℓ. The tension on the taught side becomes $T_p + T_\ell$ while the tension on the loose side becomes $T_p - T_\ell$. The torque balance equation about the axis of rotation of the input pulley can be written as

$$\tau_i - (T_p + T_\ell)r_1 + (T_p - T_\ell)r_1 = 0, \tag{1}$$

which yields

$$T_\ell = \frac{\tau_i}{2r_1}. \tag{2}$$

The tension variations in the cable occur in contact regions between the cable and the pulleys called the slip regions. These regions are represented in figure 1 with the angles θ_{s1} to θ_{s4}. Along these slip regions, the cable elongates or shortens due to the applied torque. This local variation in length causes
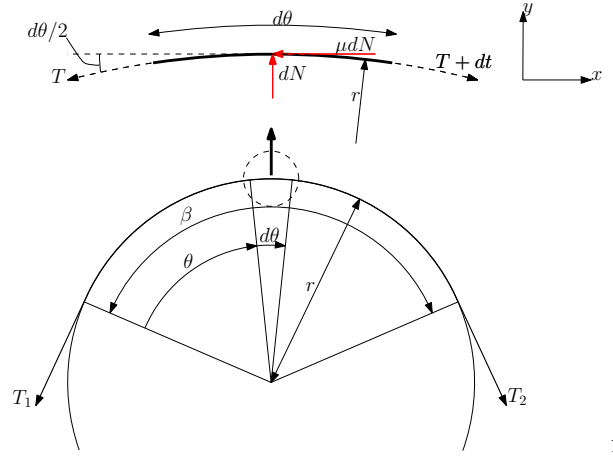
friction between the pulleys and the cable. Figure 2 illustrates this principle.

Figure 2 shows a small segment of a cable lying on the surface of a pulley of radius r. The small cable segment is lying on a small angle segment of the pulley $d\theta$. The static friction coefficient between the pulley and the cable is μ. The tension on one end of the small cable segment is T while it is $T + dT$ at the other end. The small tension variation is created by an applied torque on the pulley. The normal force between the small cable segment and the pulley is dN. When torque is applied to the pulley, the pulley surface creates a friction force on the cable segment of μdN in the tangential direction of the torque. Calculating the force balance on the cable segment gives

$$\sum F_x = T \cos\left(\frac{d\theta}{2}\right) - (T + dT)\cos\left(\frac{d\theta}{2}\right) + \mu dN = 0, \tag{3}$$

$$\sum F_y = -T \sin\left(\frac{d\theta}{2}\right) - (T + dT)\sin\left(\frac{d\theta}{2}\right) + dN = 0. \tag{4}$$

Since $d\theta$ is a small angle and dT is a small tension variation, the following approximations can be made

$$\sin\left(\frac{d\theta}{2}\right) \approx \frac{d\theta}{2}, \;\; \cos\left(\frac{d\theta}{2}\right) \approx 1, \;\; dT d\theta \approx 0. \tag{5}$$

Applying these approximations to(3) and (4) gives

$$\frac{dT}{T} = \mu d\theta. \tag{6}$$

In figure 2, when the tension varies from T_1 to T_2 where $T_2 > T_1$, the integration over the angle β of (6) gives

$$\beta = \frac{1}{\mu} \ln\left(\frac{T_2}{T_1}\right). \tag{7}$$

Angle β is referred to as the slip angle of the slip region. Integrating from T_1 to a function $T(\theta)$ over the slip region then gives

$$T(\theta) = T_1 e^{\mu\theta}, \;\; 0 < \theta < \beta. \tag{8}$$

The same can be said by integrating from the max tension T_2 to a smaller tension $T(\theta)$ over the slip region β, which gives

$$T(\theta) = T_2 e^{-\mu\theta}, \ \ 0 < \theta < \beta. \tag{9}$$

Applying (7), (8) and (9) to the slip regions in figure 1, one finds

$$T_1(\theta) = T_p e^{\mu\theta}, \ \ 0 < \theta < \theta_{s1}, \ \ \theta_{s1} = \frac{1}{\mu}\ln\left(\frac{T_p + T_\ell}{T_p}\right), \tag{10}$$

$$T_2(\theta) = (T_p + T_\ell)e^{-\mu\theta}, \ \ 0 < \theta < \theta_{s2}, \ \ \theta_{s2} = \theta_{s1}, \tag{11}$$

$$T_3(\theta) = T_p e^{-\mu\theta}, \ \ 0 < \theta < \theta_{s3}, \ \ \theta_{s3} = \frac{1}{\mu}\ln\left(\frac{T_p}{T_p - T_\ell}\right), \tag{12}$$

$$T_4(\theta) = (T_p - T_\ell)e^{\mu\theta}, \ \ 0 < \theta < \theta_{s4}, \ \ \theta_{s4} = \theta_{s3}. \tag{13}$$

Equations (10) to (13) describe the variation of the tension along the cable. These equations are used in the following section to model the stiffness of a capstan drive.

III. STIFFNESS MODEL OF A CAPSTAN DRIVE

Hooke's law gives the relationship between the tensile force in an elastic object and its strain. The strain of an elastic object is also defined as its variation in length over its original length. Expressing this definition of strain in an infinitesimal form and equating it to Hooke's law, one can then write

$$\epsilon \equiv \frac{d\delta}{dL} = \frac{F}{AE}, \Rightarrow d\delta = \frac{F dL}{AE} \tag{14}$$

where ϵ is the strain, $d\delta$ is a very small length variation, dL is a very small cable length, F is the tensile force applied on the elastic object, A is the object's cross section area and E is its Young modulus. Equation (14) can be integrated to determine the cable deformation.

The cable deformation δ_i along the slip region θ_{si} is equal to the total deformation along the slip region minus the initial deformation caused by the preload. Using (14) and using the fact that $dL = rd\theta$, the deformations δ_i are obtained as

$$\delta_i = \frac{r}{AE}\left(\int_0^{\theta_{si}} T_i(\theta)d\theta - T_p \int_0^{\theta_{si}} d\theta\right), \ \ i = 1,\dots,4 \tag{15}$$

where $r = r_2$ for θ_{s1} and θ_{s4} and $r = r_1$ for θ_{s2} and θ_{s3}. Applying (15) to the slip angle θ_{s1} gives

$$\delta_1 = \frac{T_p r_2}{AE}\left(\int_0^{\theta_{s1}} e^{\mu\theta}d\theta - \int_0^{\theta_{s1}} d\theta\right), \tag{16}$$

$$= \frac{T_p r_2}{AE}\left(\frac{1}{\mu}\left(e^{\mu\theta_{s1}} - 1\right) - \theta_{s1}\right), \tag{17}$$

$$= \frac{r_2}{\mu AE}\left(T_\ell - T_p \ln\left(\frac{T_p + T_\ell}{T_p}\right)\right). \tag{18}$$

Similarly for δ_2 to δ_4, one obtains

$$\delta_2 = \frac{r_1}{\mu AE}\left(T_\ell - T_p \ln\left(\frac{T_p + T_\ell}{T_p}\right)\right), \tag{19}$$

$$\delta_3 = \frac{r_1}{\mu AE}\left(T_\ell - T_p \ln\left(\frac{T_p}{T_p - T_\ell}\right)\right), \tag{20}$$

$$\delta_4 = \frac{r_2}{\mu AE}\left(T_\ell - T_p \ln\left(\frac{T_p}{T_p - T_\ell}\right)\right). \tag{21}$$

Some cable deformation also occurs in the cable sections which are not in contact with the pulleys. These cable sections are here called the free sections and the deformation along these sections is obtained by integrating (14) which gives

$$\delta_{f1} = \frac{T_p + T_\ell}{AE}\int_0^{L_f} dL = \frac{T_p + T_\ell}{AE}L_f, \tag{22}$$

$$\delta_{f2} = \frac{T_p - T_\ell}{AE}\int_0^{L_f} dL = \frac{T_p - T_\ell}{AE}L_f, \tag{23}$$

where δ_{f1} and δ_{f2} are the deformations on the tight and slack side respectively and L_f is the length of the free parts of the cable which are not in contact with the pulleys.

The compliance of the different cable sections can be defined as the absolute value of the variation in deformation of the cable as a function of the applied load. Mathematically, this means that the compliance of the different cable sections can be obtained by differentiating the deformation expressions in (18) to (23) with respect to T_ℓ. Furthermore, since compliance is the inverse of stiffness, one can easily obtain the stiffness of the different cable sections. For the slip regions, this gives

$$C_{si} = \left|\frac{d\delta_{si}}{dT_\ell}\right|, \ \ i = 1,\dots,4, \tag{24}$$

$$\Rightarrow C_{s1} = \frac{r_2}{AE\mu}\left(\frac{T_\ell}{T_p + T_\ell}\right) = \frac{1}{K_{s1}} \tag{25}$$

$$\Rightarrow C_{s2} = \frac{r_1}{AE\mu}\left(\frac{T_\ell}{T_p + T_\ell}\right) = \frac{1}{K_{s2}} \tag{26}$$

$$\Rightarrow C_{s3} = \frac{r_1}{AE\mu}\left(\frac{T_\ell}{T_p - T_\ell}\right) = \frac{1}{K_{s3}} \tag{27}$$

$$\Rightarrow C_{s4} = \frac{r_2}{AE\mu}\left(\frac{T_\ell}{T_p - T_\ell}\right) = \frac{1}{K_{s1}} \tag{28}$$

For the stiffnesses of the free sections of the cable, one obtains

$$K_{f1} = K_{f2} = \frac{AE}{L_f} \tag{29}$$

The total stiffness of the capstan transmission is obtained by combining the individual stiffnesses of the cable segments along the transmission. The stiffness elements K_{s1}, K_{f_1} and K_{s2} form a serial combination of springs. The same can be said for K_{s3}, K_{f_2} and K_{s4}. The two serial springs groups are in parallel to one another meaning that the total stiffness of the transmission can be written as

$$K = K_1 + K_2, \tag{30}$$

where

$$K_1 = \frac{1}{\frac{1}{K_{s1}} + \frac{1}{K_{f1}} + \frac{1}{K_{s2}}}, \tag{31}$$

$$K_2 = \frac{1}{\frac{1}{K_{s3}} + \frac{1}{K_{f2}} + \frac{1}{K_{s4}}}. \tag{32}$$

The total stiffness K represents the linear stiffness of the transmission. Since a capstan drive is a torsional element, a better indicator of its stiffness is the drive's torsional stiffness when one of its pulleys is held rigidly. The torsional stiffness K_t of the capstan drive when the small pulley is held rigidly and a torque τ is applied on the large pulley, causing an angular displacement α, is then given by

$$\tau = K_t\alpha. \tag{33}$$

The relationship between K_t and K is obtained by writing

$$\frac{\tau_D}{r_2} = K\delta \tag{34}$$

$$\alpha = \frac{\delta}{r_2}. \tag{35}$$

Equation (34) gives the relationship between a torque τ applied on the large pulley of radius r_2 and the total linear displacement δ when the small pulley is held tightly. Equation (35) gives the relationship between the total linear displacement of the cable and the angular displacement α of the large pulley of radius r_2. Using these two equations with (33) yields

$$K_t = Kr_2^2. \tag{36}$$

The following section shows how placing the capstan transmission's cable into grooves helps to increase the coefficient of friction between the cable and the pulleys and therefore the transmission's stiffness.

IV. INFLUENCE OF GROOVES ON THE CAPSTAN DRIVE STIFFNESS

Analyzing the equations for the stiffness of the different cable sections of a capstan drive ((32) to (35)), one can clearly see that all the stiffness terms are proportional to the coefficient of friction. Therefore, Increasing the coefficient of friction between the cable and the pulleys is an effective way to increase the overall stiffness of the transmission. Figure 3 illustrates how circular grooves help to increase the coefficient of friction between the cable and the capstan drive pulleys.

The illustrations in figure 3 show the distribution of the normal force occurring between a small section of the cable and a pulley groove. In figure 3a, the distribution of the normal force is considered to be uniform along the interface between the cable and the groove. The figure shows the cross section of the interface which is perpendicular to the plane shown in figure 2. The equivalent normal force between the small cable segment and the pulley segment is noted dN and can be mathematically obtained as

$$dN = \int_0^\pi \delta f \sin\phi d\phi = 2\delta f, \tag{37}$$

where ϕ is the variable angle along the interface cross section and δf is a unit force quantity. Applying Coulomb's law of static friction to the cross-section in figure 3a gives

$$dF_f = \int_0^\pi \mu df d\theta = \pi\mu df, \tag{38}$$

figuresubfloatsubfigure

a: Uniform distribution.

figuresubfloatsubfigure
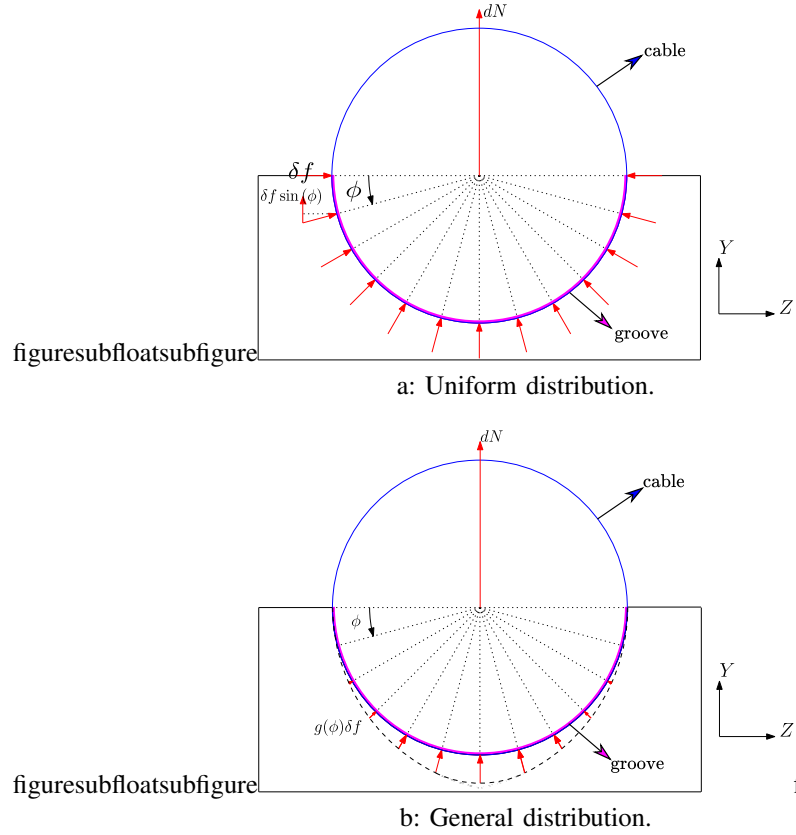
b: General distribution.

Fig. 3. Distribution of the normal force along the cross-section interface between the cable and the pulleys.

where dF_f is the friction force between the cable segment and the cable pulley. Combining (37) and (38) gives

$$dF_f = \mu' dN = \frac{\pi\mu}{2}dN, \tag{39}$$

where μ' is the effective coefficient of friction between the cable and the pulley grooves. Equation (39) shows that, when considering a uniform distribution along the cross section of the cable pulley interface, grooves can help to increase the effective friction coefficient by a factor of $\pi/2$. However, this force distribution along the interface arc is very unlikely considering the fact that local normal force around the middle of the cross-section arc is likely larger than the one at each extremity of the cross-section arc. Considering this, figure 3b shows how the force could be distributed along the cross-section arc if a general force distribution function $g(\phi)$ is considered. The effective friction coefficient given this consideration is then obtained by

$$dN = \delta f I_1(\phi) = \delta f \int_0^\pi g(\phi)\sin\phi d\phi, \tag{40}$$

$$dF_f = \mu\delta f I_2(\phi) = \mu\delta_f \int_0^\pi \mu g(\phi)d\phi. \tag{41}$$

$$dF_f = \mu' dN = \frac{\mu I_2(\phi)}{I_1(\phi)}dN. \tag{42}$$

For any type of positive distribution function $g(\phi)$, the ratio of $\frac{I_2(\phi)}{I_1(\phi)}$ will always be greater than 1. This means that a groove
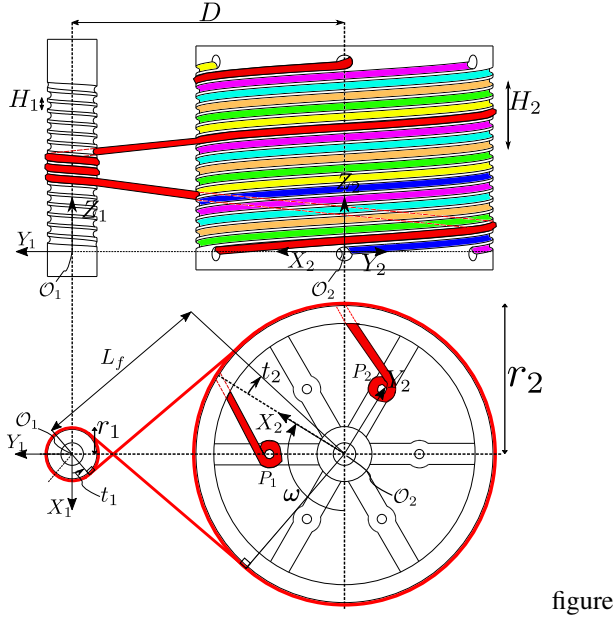
Fig. 4. Architecture of the novel capstan drive.

can only increase the effective friction coefficient between the cable and the pulleys of a capstan drive and will therefore make it stiffer.

The following section presents a novel capstan drive architecture that takes advantage of the increased effective friction coefficient of grooved pulleys and uses multiple grooves on its output pulley in order to allow different cable arrangements which further increase the stiffness of the drive.

V. NOVEL CAPSTAN DRIVE ARCHITECTURE

The novel architecture is presented in figure 4. The novel capstan drive is composed of two pulleys, the input pulley of radius r_1 which is connected to the motor and the output pulley of radius r_2 which is connected to the output of the drive. A cable indicated by a red line goes from the output pulley to the input pulley and back to the output pulley. Points P_1 and P_2 are anchoring points where the cable is fixed. The grooves on each pulley have identical cross sections. However, the groove on the input pulley forms a single helix with a pitch of H_1 while the grooves on the output pulley form a R-helix where R is the reduction ratio of the drive, i.e. r_2/r_1. In figure 4, the grooves on the output pulley are each indicated with a different colour to help differentiate them. Each of the output grooves has a pitch of H_2, where $H_2 = RH_1$. The grooves of the output pulley evolve in a direction opposite that of the grooves of the input pulley. The free cable length L_f indicates the part of the cable that is not in direct contact with either of the drive pulleys. The distance between the centre axes of the pulleys is noted D.

The presence of grooves on both the input and the output pulleys helps to increase the stiffness of the drive by increasing the effective coefficient of friction between the cable and the pulleys, as mentioned in the preceding section. Furthermore, the multiple grooves present on the output pulley enable the use of multiple cables in different cable arrangements, which

can further increase the stiffness of the drive.

Figure 5 illustrates the different possible cable arrangements. In figure 5a, a single cable is used which is fixed at both ends to the output pulley. This arrangement has the advantage of being simple and its stiffness model is equivalent to the stiffness model of a typical capstan drive such as the one presented in figure 1. This arrangement can be used many times in parallel as shown in figure 5b in order to multiply the total stiffness of the transmission. However, since none of the cables are fixed to the input pulley, slipping of the input pulley is possible.

The layout shown in figure 5c uses two cables. Each cable is fixed to the input pulley at one end and to the output pulley at the other end. This cable arrangement has the advantage of ensuring that the input pulley does not slip. However, it requires two cables to obtain a transmission stiffness which is equivalent to the transmission stiffness of a single cable arrangement in figure 5a.

The layout shown in figure 5d uses three cables. Two of its cables are fixed to both the input and output pulley while its third cable is strictly fixed to the output pulley but loops over the input pulley. The first two cables ensure the motion coupling of the input and output pulley (that there is no slipping) while the third cable helps to increase the transmission stiffness. This cable arrangement has the advantages of the two previous arrangements.

In all the cable arrangements shown in figure 5, the number of turns that can be made by the output pulley is given by

$$N = \frac{d - a}{H_1 R}, \tag{43}$$

where d and a are defined in figure 5, H_1 is the pitch of the groove on the input pulley and R is the reduction ratio of the drive. In order for the cables to pass from the input pulley to the output pulley and vice versa, geometric conditions must be met in order to ensure that the helical path described by the input groove aligns with one of the helical paths of the output pulley grooves. The following section presents a mathematical model that ensures proper alignment.

VI. ALIGNMENT OF THE INPUT AND OUTPUT GROOVES

The groove on the input pulley can best be described as a helix. The parametric helix function of the groove on the input pulley is given by

$$\mathbf{p}_1(t_1) = \begin{bmatrix} r_1 \cos t_1 \\ -r_1 \sin t_1 \\ \frac{H_1 t_1}{2\pi} \end{bmatrix} \tag{44}$$

with respect to the reference frame of the input pulley $\mathcal{O}_1$. The X_1 axis of $\mathcal{O}_1$ points towards the starting point of the helix. In (44), t_1 is the helix parameter of the trajectory. The second term of $\mathbf{p}_1(t_1)$ has a negative sign since the helix on the input pulley evolves in a direction opposite to the reference frame $\mathcal{O}_1$. Differentiating $\mathbf{p}_1(t_1)$ with respect to t_1 gives a vector that is tangent to $\mathbf{p}_1(t_1)$ and which can be written as

$$\mathbf{q}_1(t_1) = \frac{d\mathbf{p}_1(t_1)}{dt_1} = \begin{bmatrix} -r_1 \sin t_1 \\ -r_1 \cos t_1 \\ \frac{H_1}{2\pi} \end{bmatrix} \tag{45}$$
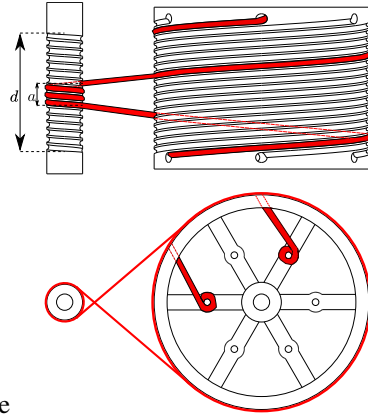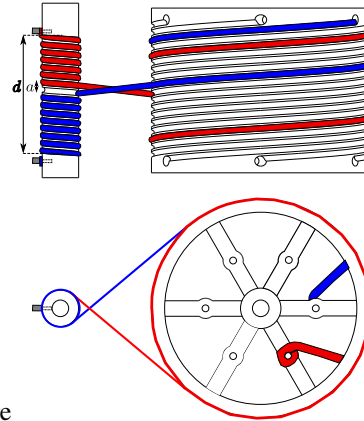
figuresubfloatsubfigure

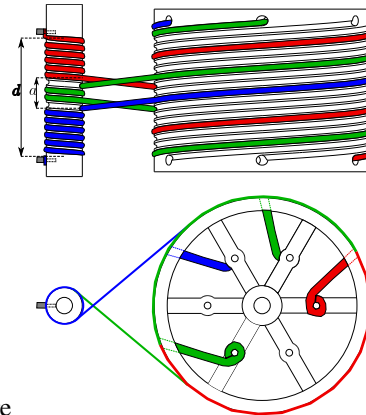a: One cable fixed at both ends to the output pulley.
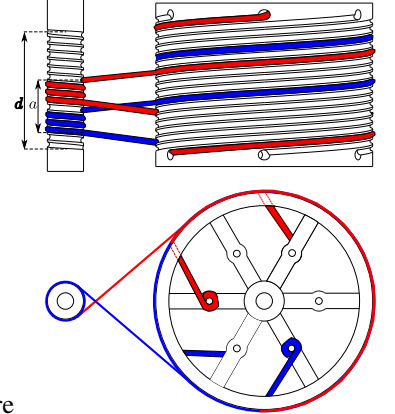
figuresubfloatsubfigure

b: Two cables both fixed at both ends to the output pulley.

figuresubfloatsubfigure

c: Two cables with ends fixed at the input pulley and the output pulley.

figuresubfloatsubfigure figure

d: Three cables, two having ends fixed at the input and output pulley and one being fixed at both ends to the output pulley.

Fig. 5. Different possible cable arrangements.

The unit vector $\mathbf{u}_1(t_1)$ along $\mathbf{q}_1(t_1)$ is obtained by dividing $\mathbf{q}_1(t_1)$ by its Euclidean norm which gives

$$\mathbf{u}_1(t_1) = \frac{\mathbf{q}_1(t_1)}{\rho_1}, \quad \rho_1 = \frac{\sqrt{H_1^2 + 4\pi^2 r_1^2}}{2\pi}. \tag{46}$$

The grooves on the output pulley can also be described by parametric helix functions. These functions can be written as

$$\mathbf{p}_{2i}(t_{2i}) = \begin{bmatrix} r_2 \cos t_{2i} \\ r_2 \sin t_{2i} \\ \frac{H_2 t_{2i}}{2\pi} \end{bmatrix}, \tag{47}$$

$$t_{2i} = t_2 + \frac{(i-1)}{R} 2\pi, \quad i = 1, \ldots, R, \tag{48}$$

with respect to the reference frame of the output pulley $\mathcal{O}_2$. The X_2 axis points towards the starting point of one of the output grooves. In (48), t_2 is the general helix parameter of the output pulley and the t_{2i} parameters are specific to each individual groove of the output pulley.

Differentiating vectors $\mathbf{p}_{2i}(t_{2i})$ with respect to t_2 gives vectors that are tangent to their respective $\mathbf{p}_{2i}(t_{2i})$ vectors. These tangent vectors can be written as

$$\mathbf{q}_{2i}(t_{2i}) = \frac{d\mathbf{p}_{2i}(t_{2i})}{dt_2} = \begin{bmatrix} -r_2 \sin t_{2i} \\ r_2 \cos t_{2i} \\ \frac{H_2}{2\pi} \end{bmatrix}, \quad i = 1, \ldots, R. \tag{49}$$

The tangent unit vectors along the $\mathbf{q}_{2i}(t_{2i})$ vectors are given by

$$\mathbf{u}_{2i}(t_{2i}) = \frac{\mathbf{q}_{2i}}{\rho_2}, \quad \rho_2 = \frac{\sqrt{H_2^2 + 4\pi^2 r_2^2}}{2\pi}, \quad i = 1, \ldots, R. \tag{50}$$

The helix functions of the input pulley groove and one of the output pulley grooves can be expressed as a function of one another in the following loop closure equation

$$\mathbf{p}_1 + L_f \mathbf{u}_1 = \mathbf{a} + \mathbf{Q}\mathbf{p}_{2i}, \quad i = 1, \ldots, R, \tag{51}$$

where $\mathbf{a} = \begin{bmatrix} 0 & -D & 0 \end{bmatrix}^T$ is a vector expressed in the $\mathcal{O}_1$ reference frame and $\mathbf{Q}$ is a rotation matrix expressing a change of reference frame from $\mathcal{O}_2$ to $\mathcal{O}_1$ and is written as

$$\mathbf{Q} = \begin{bmatrix} \cos\omega & -\sin\omega & 0 \\ \sin\omega & \cos\omega & 0 \\ 0 & 0 & 1 \end{bmatrix}, \tag{52}$$

where ω represents the amount of rotation of the output pulley needed in order to have the cables pass smoothly between the two pulleys. Equation (51) is equivalent to the three following scalar equations

$$r_1 \left(\cos t_1 - \frac{L_f}{\rho_1} \sin t_1 \right) = r_2 \cos(\omega + t_{2i}), \tag{53}$$
$$i = 1, \ldots, R,$$

$$-r_1 \left(\sin t_1 + \frac{L_f}{\rho_1} \cos t_1 \right) = -D + r_2 \sin(\omega + t_{2i}), \tag{54}$$
$$i = 1, \ldots, R,$$

$$H_1 \left(t_1 + \frac{L_f}{\rho_1} \right) = H_2 t_2. \tag{55}$$

In addition to these equations, in order to ensure the proper alignment of the input and output pulley grooves, one must be able to draw a straight line from the input groove to one of the output grooves where the line is tangent to both grooves. This can be mathematically written as

$$\mathbf{q}_1 \times \mathbf{Q}\mathbf{q}_{2i} = \mathbf{0}, \quad i = 1, \ldots, R, \tag{56}$$

which is equivalent to the following three scalar equations

$$\frac{H_2 r_1}{2\pi} \cos t_1 + \frac{H_1 r_2}{2\pi} \cos(\omega + t_{2i}) = 0, \quad i = 1, \ldots, R, \tag{57}$$

$$\frac{H_2 r_1}{2\pi} \sin t_1 - \frac{H_1 r_2}{2\pi} \sin(\omega + t_{2i}) = 0, \quad i = 1, \ldots, R, \tag{58}$$

$$\sin(t_1 + t_{2i} + \omega) = 0, \quad i = 1, \ldots, R. \tag{59}$$

From (59), we obtain that

$$t_1 + t_{2i} + \omega = n\pi, n \in \mathbb{N}, \quad i = 1, \ldots, R. \tag{60}$$

Substituting (60) into (57) and (58) yields

$$\frac{H_2 r_1}{2\pi} \cos t_1 + \frac{H_1 r_2}{2\pi} \cos(n\pi - t_1) = 0, \quad i = 1, \ldots, R, \tag{61}$$

$$\frac{H_2 r_1}{2\pi} \sin t_1 - \frac{H_1 r_2}{2\pi} \sin(n\pi - t_1) = 0, \quad i = 1, \ldots, R. \tag{62}$$

Equations (61) and (62) are both satisfied if

$$H_2 r_1 = H_1 r_2 \tag{63}$$

and

$$n = 2m + 1, \quad m \in \mathbb{N}. \tag{64}$$

Equations (60), (63) and (64) represent the conditions that must be met in order to be able to draw a straight line from the input pulley groove to one of the output pulley grooves where the line is tangent to both grooves. Substituting these conditions into (53) and (55) leads to

$$(r_2 + r_1) \cos t_1 = \frac{L_f r_1}{\rho_1} \sin t_1, \tag{65}$$

$$D - (r_2 + r_1) \sin t_1 = \frac{L_f r_1}{\rho_1} \cos t_1. \tag{66}$$

Dividing (65) by (66) and rearranging then yields

$$\sin t_1 = \left(\frac{r_2 + r_1}{D} \right). \tag{67}$$

The right-hand side term in (67) is bound between 0 and 1 since $D \in [(r_2 + r_1), \infty[$. This means that

$$t_1 = \varphi + 2\pi p, \quad p \in \mathbb{N} \tag{68}$$

or

$$t_1 = (2p + 1)\pi - \varphi, \quad p \in \mathbb{N}, \tag{69}$$

$$\varphi = \sin^{-1}\left(\frac{r_1 + r_2}{D} \right). \tag{70}$$

Substituting (69) into (65), one finds that L_f would need to have a negative length, which is impossible. This is not the case when t_1 is given by (68) and therefore this is the only possible value for t_1. The value of L_f is thus

$$L_f = \frac{\rho_1}{r_1} \sqrt{D^2 - (r_2 + r_1)^2}. \tag{71}$$

Having L_f and t_1, one can finally find the value of ω using (55) and (60) as

$$\omega = (2m+1)\pi - t_1 - \frac{\left(t_1 + \frac{L_f}{\rho_1}\right)}{R} - \frac{2\pi(i-1)}{R}, \qquad (72)$$
$$i = 1, \ldots, R, m \in \mathbb{N},$$

with t_1 given by (68) and L_f given by (71). Equation (72) can be simplified since the output pulley is $2\pi/R$ symmetric about the Z_2 axis in figure 4. The simplified version of (72) is written as

$$\omega = \left(\frac{-\left(\varphi\left(R+1\right) + \frac{L_f}{\rho_1}\right)}{R}\right) // \left(\frac{2\pi}{R}\right), \qquad (73)$$

where $a//b$ returns the remainder of a divided by b.

Angle ω varies with the distance separating the axes of the input and output pulleys D. Knowing D, properly aligning the pulleys so that the cables follow a smooth path simply requires that both pulleys be locked during the cable mounting with the large pulley being rotated by an angle ω from the X_1 axis of the small pulley around the Z_2 axis of the large pulley. After having taught all the cables at both ends, the system can then be unlocked and the pulley grooves are properly aligned. This process is better illustrated in figure 6.

VII. Multimedia Extension

A video accompanies this paper. The video demonstrates the operation of a prototype of the novel capstan drive as well as its backdrivability.

VIII. Conclusion

This paper presented a novel capstan drive architecture which uses grooves on both its input and output pulleys in order to increase the effective coefficient of friction between the drive cables and the pulleys. Using a previously established model of a capstan drive, it was shown that increasing the coefficient of friction between the drive cables and the drive pulleys increases the drive stiffness, which is an important property in several applications, including for instance physical human-robot interaction. Furthermore, the many grooves on the output pulley enable multi-cable arrangements which can even further increase the transmission's stiffness. A method to ensure that the drive cables can pass smoothly between the input and output pulley was also described.

Future work on this novel capstan drive will consist in testing the established model in a test bench in order to quantify the increased coefficient of friction caused by the grooves as well as to quantify the increase in drive stiffness compared to a standard capstan drive. Furthermore, the influence of the increased drive stiffness on the drive's bandwidth will be analyzed and compared to other small-ratio transmissions in order to determine if this novel drive is advantageous for physical human robot interaction.

References

[1] L. Roveda, N. Pedrocchi, M. Beschi, and L. M. Tosatti, "High-accuracy robotized industrial assembly task control schema with force overshoots avoidance," *Control Engineering Practice*, vol. 71, pp. 142–153, 2018.

[2] D.-W. I. J. Meißner, M. S. F. Schmatz, D.-I. F. Beuß, D.-W. I. J. Sender, I. W. Flügge, and D.-K. F. E. Gorr, "Smart human-robot-collaboration in mechanical joining processes," *Procedia Manufacturing*, vol. 24, pp. 264–270, 2018.

[3] M. Raessa, D. Sánchez, W. Wan, D. Petit, and K. Harada, "Teaching a robot to use electric tools with regrasp planning," *CAAI Transactions on Intelligence Technology*, vol. 4, no. 1, pp. 54–63, 2019.

[4] C. Loughlin, A. Albu-Schäffer, S. Haddadin, C. Ott, A. Stemmer, T. Wimböck, and G. Hirzinger, "The dlr lightweight robot: design and control concepts for robots in human environments," *Industrial Robot: an international journal*, 2007.

[5] G. Xiaoqing and W. Jidong, "Mechanical design and kinematic analysis of a new kind of palletizing robot," in *2011 Second International Conference on Mechanic Automation and Control Engineering*. IEEE, 2011, pp. 404–408.

[6] 3d systems, "Phantom premium," On the WWW, August 2020, uRL https://www.3dsystems.com/haptics-devices/3d-systems-phantom-premium.

[7] K. Wen, D. Harton, T. Laliberté, and C. Gosselin, "Kinematically redundant (6+ 3)-dof hybrid parallel robot with large orientational workspace and remotely operated gripper," in *2019 International Conference on Robotics and Automation (ICRA)*. IEEE, 2019, pp. 1672–1678.

[8] K. Wen, T. S. Nguyen, D. Harton, T. Laliberté, and C. Gosselin, "A backdrivable kinematically redundant (6+3)-degree-of-freedom hybrid parallel robot for intuitive sensorless physical human–robot interaction," *IEEE Transactions on Robotics*, pp. 1–17, 2020.

[9] F. Gosselin, F. Ferlay, S. Bouchigny, C. Mégard, and F. Taha, "Specification and design of a new haptic interface for maxillo facial surgery," in *2011 IEEE International Conference on Robotics and Automation*. IEEE, 2011, pp. 737–744.

[10] J. Perret and P. Vercruysse, "Advantages of mechanical backdrivability for medical applications of force control," in *Workshop on Computer/Robot Assisted Surgery (CRAS)*, 2014.

[11] R. Baumann and R. Clavel, "Haptic interface for virtual reality based minimally invasive surgery simulation," in *Proceedings. 1998 IEEE International Conference on Robotics and Automation (Cat. No. 98CH36146)*, vol. 1. IEEE, 1998, pp. 381–386.

[12] C. R. Carignan and K. R. Cleary, "Closed-loop force control for haptic simulation of virtual environments," 2000.

[13] O. Baser and E. I. Konukseven, "Kinematic model calibration of a 7-dof capstan-driven haptic device for pose and force control accuracy improvement," *Proceedings of the Institution of Mechanical Engineers, Part C: Journal of Mechanical Engineering Science*, vol. 227, no. 6, pp. 1328–1340, 2013.

[14] W. T. Townsend, "The effect of transmission design on force-controlled manipulator performance," Ph.D. dissertation, 1988.

[15] B. Rooks, "The harmonious robot," *Industrial Robot: An International Journal*, vol. 33, no. 2, pp. 125–130, 2006.

[16] S. Phan, A. Lioulemes, C. Lutterodt, F. Makedon, and V. Metsis, "Guided physical therapy through the use of the barrett wam robotic arm," in *2014 IEEE International Symposium on Haptic, Audio and Visual Environments and Games (HAVE) Proceedings*. IEEE, 2014, pp. 24–28.

[17] Y. Lu, H. Liao, M. Hei, H. Liu, and D. Fan, "Development of a differential cable drive mechanism for acquiring tracking and pointing application," *Proceedings of the Institution of Mechanical Engineers, Part C: Journal of Mechanical Engineering Science*, vol. 229, no. 17, pp. 3191–3200, 2015.

[18] Y. Lu and D. Fan, "Non-intervene cable wrapping method for precise cable drive," in *2012 international conference on optoelectronics and microelectronics*. IEEE, 2012, pp. 378–383.

[19] ——, "Transmission backlash of precise cable drive system," *Proceedings of the Institution of Mechanical Engineers, Part C: Journal of Mechanical Engineering Science*, vol. 227, no. 10, pp. 2256–2267, 2013.
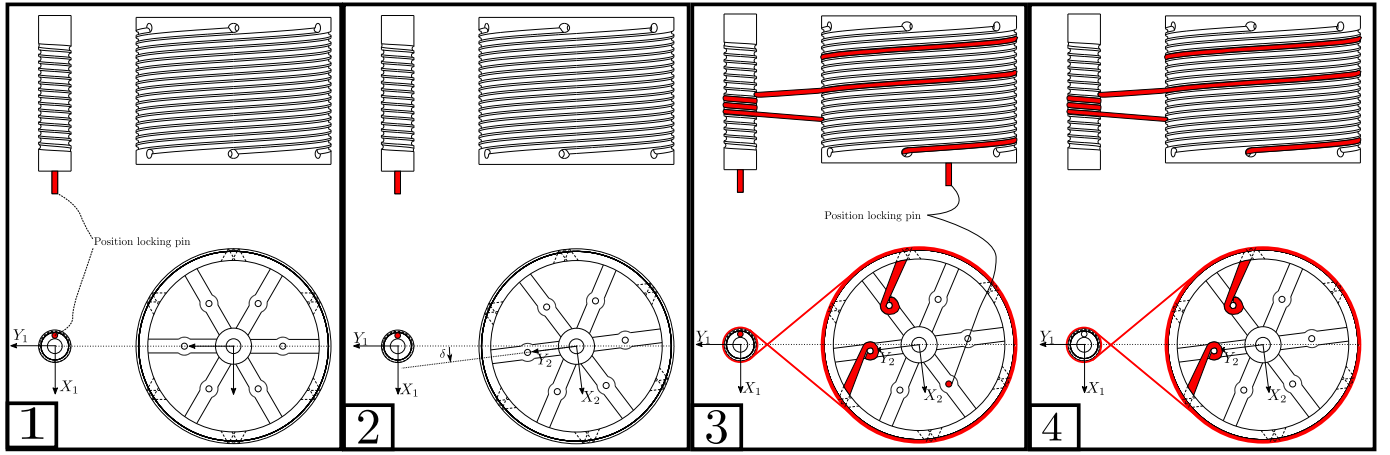
figure

Fig. 6. Steps to align the drive pulleys for smooth cable trajectories.

[20] X. Xie, C. Qi, L. Zhang, and D. Fan, "Analytical and experimental research on transmission backlash in precise cable drive for an electro-optical targeting system," *Advances in Mechanical Engineering*, vol. 11, no. 7, p. 1687814019866059, 2019.

[21] T. L. Brooks, "Telerobotic response requirements," in *1990 IEEE International Conference on Systems, Man, and Cybernetics Conference Proceedings*. IEEE, 1990, pp. 113–120.

[22] D. V. Gealy, S. McKinley, B. Yi, P. Wu, P. R. Downey, G. Balke, A. Zhao, M. Guo, R. Thomasson, A. Sinclair *et al.*, "Quasi-direct drive for low-cost compliant robotic manipulation," in *2019 International Conference on Robotics and Automation (ICRA)*. IEEE, 2019, pp. 437–443.

[23] O. Baser and E. I. Konukseven, "Theoretical and experimental determination of capstan drive slip error," *Mechanism and Machine Theory*, vol. 45, no. 6, pp. 815–827, 2010.

[24] J. Werkmeister and A. Slocum, "Theoretical and experimental determination of capstan drive stiffness," *precision Engineering*, vol. 31, no. 1, pp. 55–67, 2007.